ELSEVIER

Journal of Fluids and Structures 20 (2005) 533–554

JOURNAL OF
FLUIDS AND
STRUCTURES

www.elsevier.com/locate/jfs

Numerical investigation of flow patterns for staggered cylinder pairs in cross-flow

M.H. Akbari[1], S.J. Price*

Department of Mechanical Engineering, McGill University, Montréal, Québec, Canada H3A 2K6

Received 16 June 2004; accepted 14 February 2005
Available online 10 May 2005

Abstract

Numerical simulations of the flow patterns around two staggered circular cylinders in cross-flow are presented for the low subcritical Reynolds number regime. The unsteady two-dimensional Navier–Stokes equations for this flow are solved using a numerical vortex method, which is described in some detail. Detailed numerical results for the flow patterns for different arrangements of the cylinders, at a Reynolds number, $\mathrm{Re} = 800$, are presented and compared with existing experimental data. Five distinct flow regimes, depending on the geometrical arrangement of the cylinders, are identified in the simulations, the flow characteristics of the different regimes are discussed in some detail. For the most part, the flow patterns discerned in the numerical investigation are in agreement with previously reported experimental observations, although in some cases the flow patterns are obtained for slightly different cylinder configurations.

Keywords: Cylinder pairs in cross-flow; Vortex methods

---

1. Introduction

Study of the cross-flow over circular cylinders in different arrangements has received considerable attention from both engineering and fundamental-fluid-dynamics perspectives for close to a century now. This can be explained by the presence of this type of flow in many engineering applications, such as: heat exchangers, offshore structures, and transmission lines. Furthermore, flow over circular cylinders encompasses an array of different fundamental fluid-dynamic phenomena, such as: boundary-layer separation, shear-layer development, and vortex dynamics.

A staggered arrangement represents the most general form of a pair of cylinders in a fluid flow. Despite this, the general staggered configuration has not been studied as extensively as the simpler tandem and side-by-side configurations. However, a number of high-quality experimental investigations of the fluid dynamics for staggered cylinders can be found in the literature; for example: Suzuki et al. (1971), Ishigai et al. (1972), Price (1976), Kiya et al. (1980), Price and Païdoussis (1984), Zdravkovich (1987), Gu and Sun (1999) and Sumner et al. (2000). A limited number of numerical investigations of this problem are also available; for example: Mittal et al. (1997), Su et al. (2002) and Jester and Kallinderis (2003).

---

*Corresponding author.
E-mail address: stuart.price@mcgill.ca (S.J. Price).

[1] Presently at Shiraz University, Shiraz, Iran.

doi:10.1016/j.jfluidstructs.2005.02.005

The experimental investigations previously mentioned revealed many complexities in the fluid flow behaviour over a pair of staggered cylinders. A number of these investigations resulted in the identification of different types of flow pattern or behaviour for different arrangements of cylinders. For example, Zdravkovich (1987) suggested three primary categories of flow behaviour: proximity interference, wake interference, and combined proximity and wake interference. Gu and Sun (1999) identified three types of interference, referred to as wake interference, shear-layer interference, and neighbourhood interference. In a more recent investigation by Sumner et al. (2000), the flow over a pair of staggered cylinders was classified into nine categories. Three flow patterns were associated with cylinders in very close proximity to each other, three were attributed to configurations with small angles of incidence (the angle between the flow direction and a line connecting the centres of the two cylinders), and three were identified for configurations with large angles of incidence.

Sumner et al. (2000) reported that, when the two cylinders were located very close to each other, the combined geometry behaved in a manner similar to that of a single bluff-body, and a single Kármán vortex street was observed behind the pair of cylinders. At small angles of incidence for this bluff-body type flow, although the shear-layer shed from the downstream cylinder formed regular Kármán vortices, the shear-layer from the upstream cylinder was stretched in the flow direction, leading to interruptions in the vortex formation from this shear-layer. For larger angles of incidence, again for the bluff-body type flow, the lengths of the two shear-layers were similar, and more regular vortex shedding was reported from the two shear-layers. The last flow pattern in this category occurred for configurations with a small gap between the two cylinders and high angles of incidence. In this case, little flow was observed through the gap between the cylinders.

Sumner et al. (2000) also identified three flow patterns for small angles of incidence. In the first flow pattern, for small pitch ratios, the shear-layer originating from the upstream cylinder reattached on the outer side of the downstream cylinder—effectively preventing flow through the gap between the cylinders. Vortex shedding occurred from the other shear-layer, shed from the outer side of the upstream cylinder. The second flow pattern was obtained for slightly larger angles of incidence. In this case the shear-layer from the inner side of the upstream cylinder was deflected into the gap between the two cylinders. This shear-layer rolled up in the gap and produced small-scale Kármán vortices. This flow pattern was referred to as "induced separation". The last flow pattern for small angles of incidence occurred for larger pitch ratios. For these configurations the shear-layers shed from the upstream cylinder had sufficient space to roll up and form Kármán vortices before reaching the downstream cylinder. These Kármán vortices then impinged on the downstream cylinder, influencing both the vortex shedding from this cylinder and the overall wake structure.

For larger angles of incidence, Sumner et al. (2000) also observed three flow patterns. For these configurations there was always some flow through the gap between the cylinders, and vortex shedding occurred from both cylinders. For a wide range of angles of incidence and pitch ratios "synchronized vortex shedding" was observed. Here, the vortex shedding from the two sides of the gap synchronized, resulting in two anti-phase Kármán vortex streets in the wake of the cylinders. The other two flow patterns for larger angles of incidence were reported for smaller pitch ratios. The first occurred when the two gap-vortices paired at the gap exit, forming a counter-rotating vortex pair, which was then enveloped by the Kármán vortex from the outer side of the upstream cylinder. In this flow pattern the enveloping process was complete. However, when the enveloping process was not complete, it resulted in splitting of the vortex pair. This was the second, and most dominant flow pattern for the smaller pitch ratio configurations.

2. Numerical approach

The numerical algorithm developed and applied in this investigation is based on a vortex method described in detail by Akbari and Price (1997, 2000, 2003) and Akbari (1999). The motion of an incompressible, viscous fluid in two dimensions is described by the continuity and Navier–Stokes equations. These equations can be cast in terms of vorticity and a stream function as follows:

$$\frac{\partial\omega}{\partial t} + (\mathbf{u}\cdot\boldsymbol{\nabla})\omega = \nu\nabla^2\omega, \tag{1}$$

$$\nabla^2\psi = -\omega, \tag{2}$$

where ω, ψ, and $\mathbf{u}$ are the vorticity, stream function, and velocity vector, respectively, and ν is the kinematic viscosity of the fluid. Given the vorticity field, Eq. (2) can be solved for the stream function, the spatial derivatives of which give the velocity components. In a vortex method Eq. (1) is split into the convection and diffusion parts as follows:

$$\frac{\partial\omega}{\partial t} = -(\mathbf{u}\cdot\boldsymbol{\nabla})\omega, \tag{3}$$

$$\frac{\partial\omega}{\partial t} = \nu\nabla^2\omega. \tag{4}$$

The time domain is discretized into small time-steps, during which Eqs. (3) and (4) are solved sequentially, rather than simultaneously. Eq. (3) states that the total derivative of vorticity is zero, or that the vorticity of a fluid particle is conserved. Therefore, the vorticity domain is discretized into vortex particles, and the trajectory of these vortex particles is then dictated by the velocity field. This process provides us with a unique solution to Eq. (3). A solution to Eq. (4) is obtained by giving random walks to the vortex particles, as proposed by Chorin (1973). These random displacements are taken from two independent Gaussian distributions, each with zero mean and variance of $2\nu\Delta t$, where Δt is the time-step size.

To obtain the velocity field for convecting the vortex particles, Eq. (2), which is the Poisson equation for the stream function, is solved. A ''fast elliptic solver'', as outlined by Akbari (1999) and Swarztrauber and Sweet (1975), is used to solve the Poisson equation on a polar grid around a cylinder.

The ''no-slip'' boundary condition on the cylinder surface is satisfied through the generation of new vorticity on the solid boundary during each time-step. The total amount of vorticity generated on each segment of the surface is proportional to the tangential component of the induced velocity at that point prior to the creation of the vorticity. The ''no-flow'' boundary condition is satisfied by adjusting the Dirichlet boundary conditions of the stream function on the cylinder surface. These boundary values are calculated at the cylinder surface by integrating the desired normal velocity, which for fixed cylinders is zero. A full description of the method is given by Akbari (1999) and Akbari and Price (2000).

In the present investigation, the Poisson equation is solved using two polar grids associated with the two circular cylinders; see Fig. 1. All the vortex particles in the flow field, originating from both cylinders, are distributed onto each grid, and the boundary conditions for the stream function are calculated in the usual way. The velocity field due to the total vorticity is obtained in each polar grid separately by solving the Poisson equation for the stream function as if the other cylinders were not present. However, this procedure does not take into account the ''presence'' of the other cylinder. Therefore, in order to include the effect of the other cylinder, the velocity field on each polar grid for each cylinder must be corrected. This correction term is obtained through a distribution of sources on the surface of the other cylinder. To do this, the normal velocity component at n collocation points on the surface of each cylinder is obtained using the stream function corresponding to the other cylinder. Then a source distribution is sought on each cylinder surface such that the velocity induced by this source distribution cancels out the normal velocity components induced by the other cylinder. This leads to a system of n linear equations, with the strength of the sources on the cylinder (at n collocation points) as the unknowns, the influence of the ith source at the jth collocation point as the $a(i, j)$ coefficient, and the induced normal velocities (at the same n collocation points) are the known terms in the equations. During each time-step only the normal velocities need to be updated. This linear system is solved using the LU decomposition

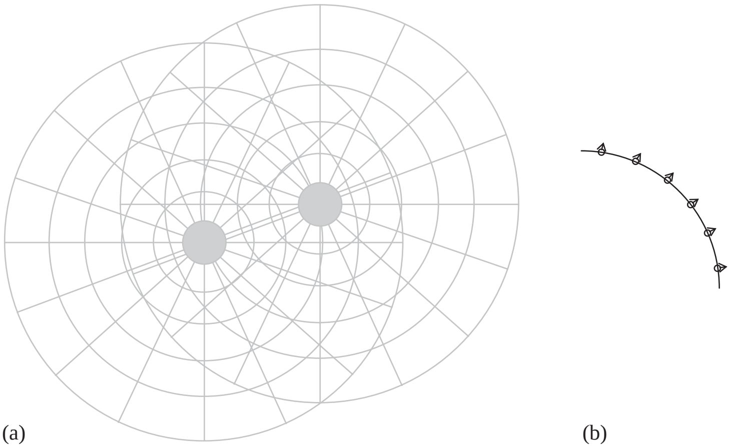

Fig. 1. A schematic of: (a) the two polar grids, and (b) the source distribution on the cylinders used in the present numerical scheme.

technique with partial pivoting. In order to prevent the singular behaviour of a point source in the vicinity of its core, each source distribution is placed at a radius just inside the cylinder (approximately at 99.999% of the cylinder radius).

When calculating the velocity field in a polar grid associated with one cylinder, the effects of the source terms from the other cylinders are accounted for. The velocity at a given point in the flow field has the same value in either polar grid, as long as the mesh densities of the two grids are similar in that neighbourhood. The rationale behind using two separate grids for the two cylinders, however, is to obtain the same resolution of fine mesh, and therefore the same accuracy in the velocity field, in the vicinity of each of the cylinders. In practice, the velocity field is calculated using only one of the grids (with the corresponding source distribution on the other cylinder) all over the domain, except within a given radius around the other cylinder. This radius is taken as half the distance between the two cylinders. Inside this region the velocity is calculated using the second grid and the corresponding source distribution (on the first cylinder).

The numerical algorithm described in the preceding can be summarized as follows.

1. At the beginning of a new time-step, distribute all vortices onto grid 1 (corresponding to cylinder 1).
2. Apply the "no-flow" boundary condition on the cylinder surface and solve Poisson's equation for the stream function on grid 1.
3. Repeat steps 1 and 2 for grid 2 (corresponding to cylinder 2).
4. With the stream function for grid 1, calculate the tangential velocity components on cylinder 1.
5. Given these tangential velocities, create new vorticity on cylinder 1 to satisfy the "no-slip" boundary condition on its surface.
6. With the stream function for grid 1, calculate the normal velocity components on the surface of cylinder 2.
7. Create the necessary source distribution on cylinder 2 to cancel out any normal velocity components calculated in the previous step.
8. Repeat steps 4 to 7 for grid 2 (exchanging 1 and 2 in those steps).
9. Distribute all vortices (including the newly generated ones on both cylinders) onto grid 1.
10. Apply the "no-flow" boundary condition on cylinder 1 and solve Poisson's equation for the stream function on grid 1. Note that in this stage of the calculation of the surface velocity components the effects of the newly generated source distribution on cylinder 2 are also included.
11. Repeat steps 9 and 10 for grid 2 (exchanging 1 and 2 in those steps).
12. Calculate the velocity field on grid 1 given the stream function calculated in step 10 and the source distribution on cylinder 2 obtained in step 7.
13. Repeat step 12 for cylinder 2 (exchanging 1 and 2 in that step).
14. Convect vortices in the flow using either of the velocity fields calculated in steps 12 and 13. Near each cylinder use the corresponding grid, and away from both cylinders use either grid.
15. Diffuse the vorticity field by giving each vortex particle a random walk.
16. Discard any vortices that have entered into the cylinders (due to random walks) or that have moved a given long distance away from the cylinders.
17. Increment the time and repeat steps 1 to 16 in the new time-step.

It is noted here that for the distribution of vorticity on a grid a bilinear interpolation scheme is applied. In all simulations reported here, the radius of the coarse polar grids was taken equal to $200D$, and that of the fine polar grids equal to $100D$ [see Akbari (1999) or Akbari and Price (1997) for details]. Also, 200×340 grids with an expansion factor of 1.2 in the radial direction, and a constant time-step size of $\Delta t^* \equiv \Delta t U/D = 0.02$ were used in all simulations. The smallest grid size (near the surface of the cylinders) is approximately $0.0025D$; considering the boundary layer thickness to be of the order of $0.1D$ at the position of maximum frontal cross-sectional area there are at least 20 grid points inside the boundary layer at this point. Both the time-step and grid size were checked for convergence during preliminary tests of the numerical scheme. A full validation of the numerical scheme is given by Akbari and Price (1997) and Akbari (1999); however, suffice it to say that either halving the time-step or doubling the number of grid nodes had no significant effect on the numerical results obtained from the simulation.

In terms of computational efficiency this numerical method is superior to more conventional Navier–Stokes solvers based on the primitive variables. This is an intrinsic characteristic of the method, since the governing partial differential equations are cast in the form of elliptic equations which are solved using a fast, direct solver, as opposed to dealing with the original equations which have to be solved by an iterative method.

In the present application of the vortex method, no turbulence model is implemented in the numerical scheme. However, in general, there are options available to include a turbulence model into the numerical scheme; see, for example, Smith and Stansby (1989).

3. Flow visualization simulation results

In this section the flow visualization results obtained from the current numerical investigation are presented.

Shown in Fig. 2 is a schematic of the two cylinders of equal diameter, D, with a centre-to-centre distance P. The angle between the mean flow direction and a line connecting the centres of the two cylinders, the angle of incidence, is denoted by α. The geometry of the cylinder pair can also be expressed in terms of the longitudinal (direction of the mean flow) and transverse spacing between the cylinders, denoted by L and T, respectively, in Fig. 2.

The Reynolds number in all the simulations reported here was fixed at $\mathrm{Re} = 800$. A series of flow visualization animation videos were produced from the simulations, which were used to study the flow behaviour for different configurations of the pair of staggered cylinders. The locus of the 25 staggered configurations investigated in this study is shown in Fig. 3.

We were able to identify five basic flow regimes in our simulations: base-bleed flow, shear-layer reattachment, vortex pairing and enveloping, vortex impingement, and complete vortex shedding. Each of these flow regimes is discussed in some detail in the following sections. The approximate regions in which these different flow regimes are observed are indicated in Fig. 3. For some cylinder configurations the flow did not fully demonstrate the characteristics of any one of the identified flow regimes; instead the wake structure exhibited a transition between two or more of the regimes. These cases are indicated in Fig. 3 by points that are outside of the specified regions.

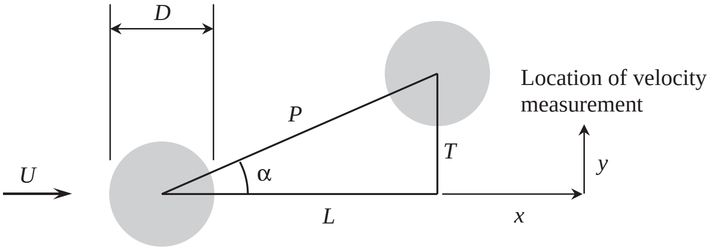

Fig. 2. A schematic of two circular cylinders in staggered arrangement in a cross-flow.

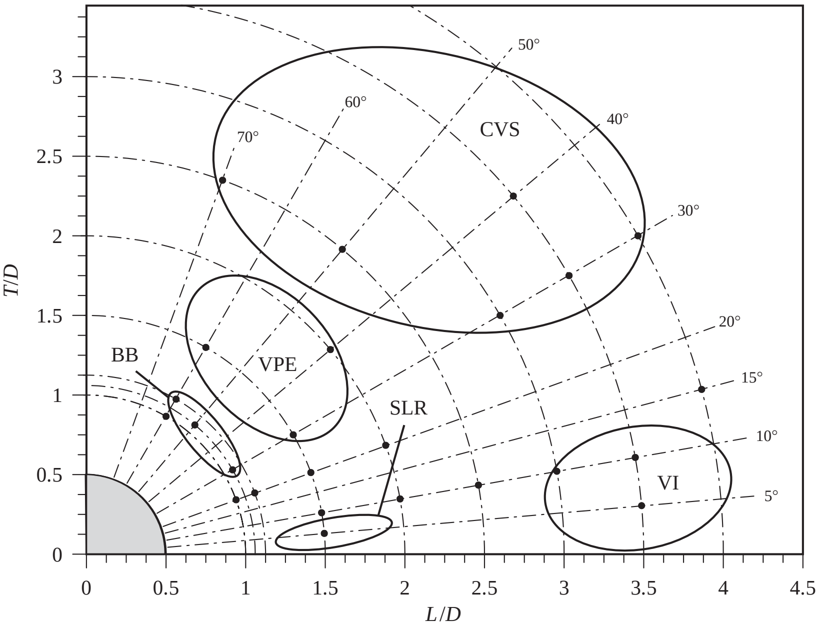

Fig. 3. Locus of the configurations investigated in the present study; different positions of the downstream cylinder are indicated by the symbol ●. Also indicated are the approximate regions for different types of flow behaviour: BB, base-bleed; SLR, shear-layer reattachment; VPE, vortex pairing and enveloping; VI, vortex impingement; CVS, complete vortex shedding.

The numerical results of this study, obtained at a Reynolds number of 800, are compared primarily with the experimental results of Sumner et al. (2000), obtained for Reynolds numbers in the range 850–1900. It is noted that our numerical simulations are strictly two-dimensional, while three-dimensional effects may be present in the flow at Reynolds numbers as low as 200. However, we expect that 3-D effects will not be dominant at a low subcritical Reynolds number of 800; this is also suggested by the experimental results of Sumner et al. (2000).

3.1. Base-Bleed Flow

This flow behaviour was observed for small pitch ratios and large angles of incidence, approximately $P/D \leqslant 1.1$ and $\alpha \geqslant 30^\circ$. In this flow regime a narrow jet of fluid flows through the gap between the two cylinders. The inclination of this jet toward the upstream cylinder disrupts the roll-up of the shear-layer from the outer surface of that cylinder, causing it

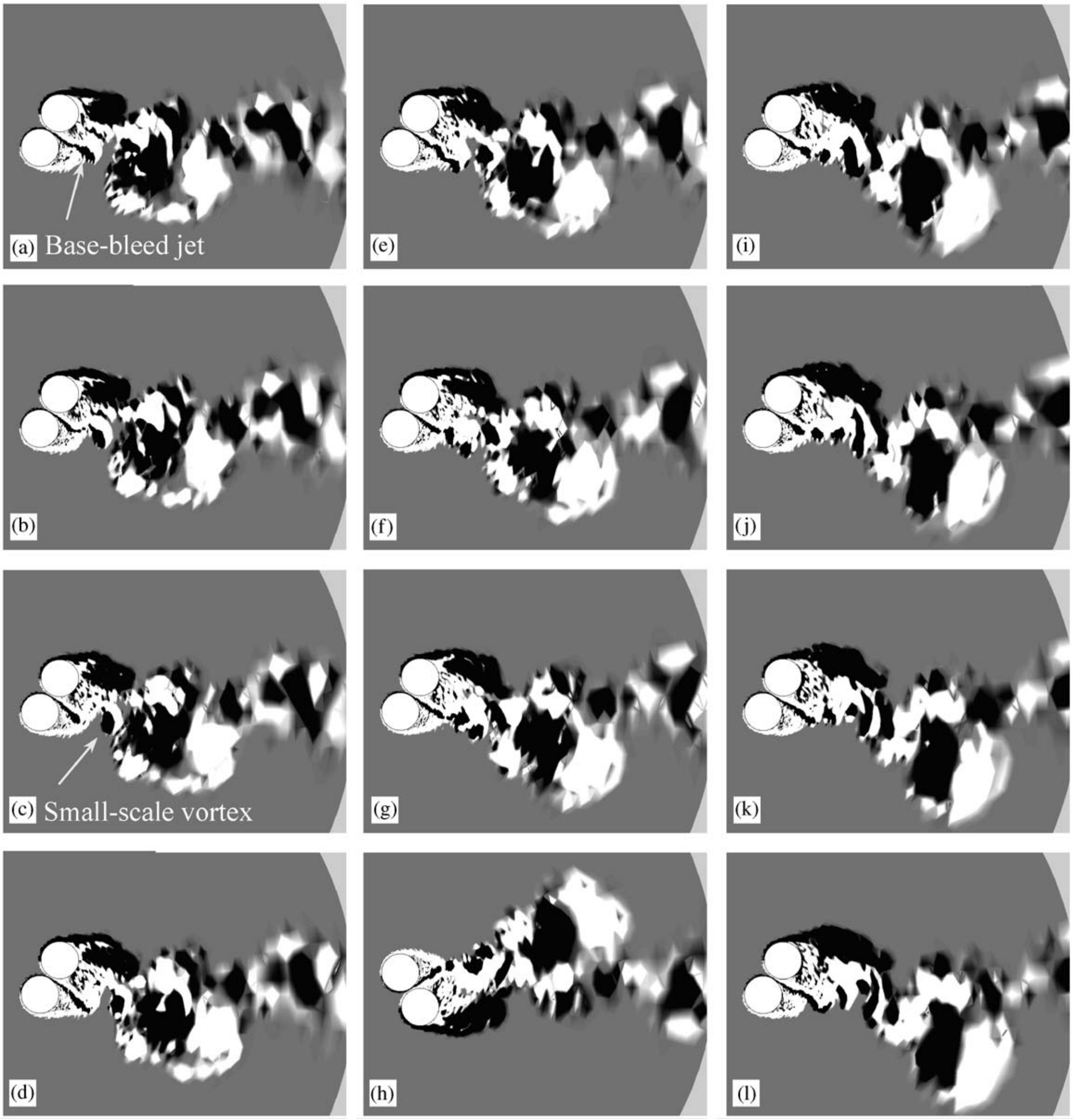

Fig. 4. Vorticity contour plots for a "base-bleed" flow regime with $P/D = 1.06$, $\alpha = 60^\circ$, $\mathrm{Re} = 800$. Equal time-intervals of $t^* \equiv tU/D = 0.2$ between consecutive plots (a)–(l).

to produce small-scale vortex structures that prevent regular formation of Kármán vortices in the wake. The wake structure in this flow regime is thus disorganized.

Shown in Fig. 4 are vorticity contour plots and in Fig. 5 numerical flow visualization plots (streaklines) at several instances for a base-bleed flow regime with $P/D = 1.06$ and $\alpha = 60^\circ$. The time-interval between consecutive plots is $t^* \equiv tU/D = 0.2$, where t is time and U is the free-stream velocity. As seen in these figures, the wake structure is not well organized; a Kármán vortex street cannot be identified in the wake region. The outer shear-layer from the downstream cylinder does, however, still manage to form almost regular vortices. The regular shape of these vortices is destroyed in the immediate near-wake region by the action of high-frequency small-scale vortices formed by the base-bleed jet. The high frequency of these small-scale vortices can be realized by inspecting Figs. 4(a–d) and 5(a–d), for example, which show the formation of one such vortex. This time-scale should be compared with that for the formation of a large-scale vortex from the outer shear-layer of the downstream cylinder; Figs. 4(a–l) and 5(a–l) cover only about half the time

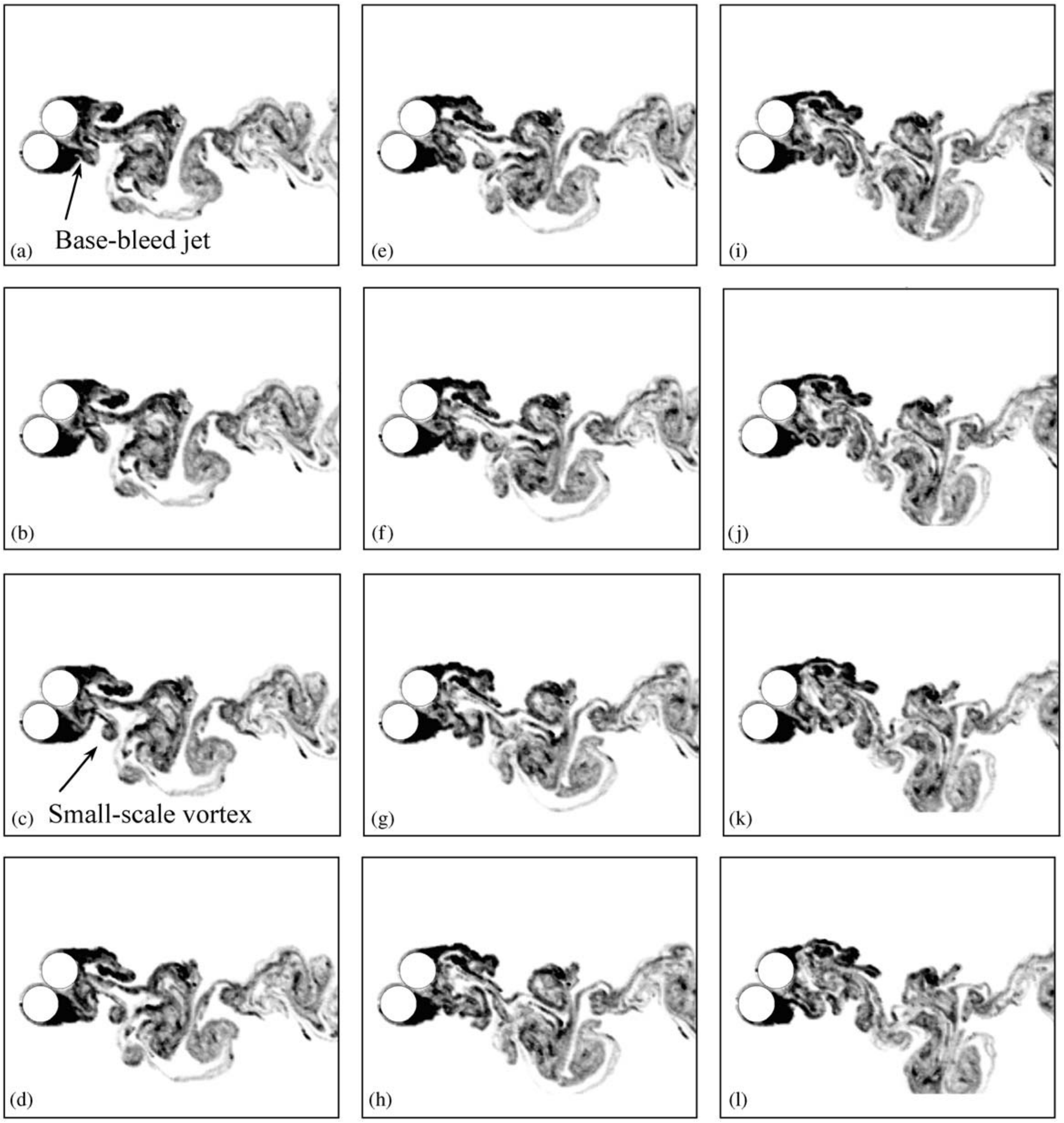

Fig. 5. Numerical flow visualization plots (streaklines) for a “base-bleed” flow regime with $P/D = 1.06$, $\alpha = 60^\circ$, Re $= 800$. Equal time-intervals of $t^* \equiv tU/D = 0.2$ between consecutive plots (a)–(l).

required for the formation of one such large-scale vortex. Nonetheless, a dominant peak at the nondimensional frequency of $fD/U \approx 0.18$ is obtained in the wake PSD for this case. It is worth mentioning that a Strouhal number of about 0.185 was obtained in our simulation for a single cylinder in a cross-flow at the same Reynolds number [see Akbari (1999) and Akbari and Price (1997)].

Since our primary objective in the present work was the identification of flow patterns over cylinders, no attempt was made to calculate either the pressure distribution or the total fluid force acting on the cylinders. However, it is expected that the disruption of regular vortex shedding from the upstream cylinder will significantly modify the base pressure of the cylinder, and result in a significant reduction in the alternating component of the drag force acting on the upstream cylinder [see, for example, Bearman (1967)].

3.2. Shear-Layer Reattachment

For configurations with moderate pitch ratios, $1.1 < P/D < 2$, and small angles of incidence, $\alpha < 10^\circ$, the downstream cylinder is within the wake of the upstream cylinder. The distance between the two cylinders is small enough for the inner shear-layer from the upstream cylinder to reattach onto the outer surface of the downstream cylinder. The flow through the gap between the cylinders is small compared to the bulk, main flow around the two cylinders. There is only one Kármán vortex street in the wake of the pair of cylinders. This flow pattern was identified previously by Sumner et al. (2000) for staggered cylinders, and was also mentioned by Zdravkovich (1987) as a form of "wake interference" for tandem arrangements ("W-T2" flow regime).

Fig. 6(a) shows streamlines from the current numerical study for a case with $P/D = 1.5$, $\alpha = 5^\circ$, and $\mathrm{Re} = 800$, and Fig. 6(b) depicts an experimental flow visualization image taken from Sumner et al. (2000) for a shear-layer reattachment case with $P/D = 1.5$, $\alpha = 10^\circ$, and $\mathrm{Re} = 1300$. (Note that in the simulation with $P/D = 1.5$ and $\alpha = 10^\circ$ a shear-layer reattachment flow pattern was not observed as clearly as that with $\alpha = 5^\circ$.) The two plots have many similarities in the flow pattern details, such as the length of the shear-layers and location of the vortices in the wake. Shown in Fig. 7 is the wake power spectrum obtained from the numerical simulations with $P/D = 1.5$, $\alpha = 5^\circ$, and $\mathrm{Re} = 800$ (Fig. 6(a)). As seen, the dominant (nondimensional) wake frequency, or Strouhal number, is approximately 0.21. Sumner et al. (2000) did not report a Strouhal number for cylinder configurations in this range; however, Kiya et al. (1980) reported $\mathrm{St} \approx 0.19$ for $P/D = 1.5$, $\alpha = 0^\circ$, and $\mathrm{Re} = 17\,000$.

Shown in Figs. 6(c) and (d), respectively, are the numerical and experimental flow visualization results for $P/D = 2.0$ and $\alpha = 10^\circ$. Sumner et al. (2000) reported a shear-layer reattachment flow regime for this geometry. This was not obtained as clearly in the numerical simulations as that indicated in the experimental results. However, the numerical simulations did indicate a single Kármán vortex street in the wake of the cylinders, which was similar to that observed in the corresponding experimental study.

An examination of the simulation results for $P/D = 1.5$, $\alpha = 10^\circ$ and $P/D = 2.0$, $\alpha = 10^\circ$ suggests that these flows may fall within the "induced-separation" flow regime of Sumner et al. (2000), which they identified for larger angles of incidence ($\alpha > 10^\circ$). Nonetheless, it is noted that according to our simulations the so-called "induced-separation" phenomenon indicated by Sumner et al. (2000) does not appear to be really an "induced" separation; the separation on the inner face of the downstream cylinder appears to be due to the impingement of part of the main flow through the gap and its subsequent deflection off the cylinder surface. This can easily be recognized by considering the numerical flow visualization simulations and experimental results from two configurations which Sumner et al. (2000) identified as belonging to the "induced-separation" regime; these are compared in Fig. 8. It is clear from the numerical results that the streamlines separating from the inner surface of the downstream cylinders in Figs. 8(a, c) originate from the main incoming flow rather than from the shear-layer of the inner side of the upstream cylinder. On the other hand, it is not obvious from the experimental flow visualization, shown in Figs. 8(b, d), that the flow separation on the front side of the downstream cylinder is indeed induced by the shear-layer from the inner surface of the upstream cylinder, as postulated by Sumner et al. (2000).

3.3. Vortex Pairing and Enveloping

For cylinder configurations with moderate pitch ratios and high angles of incidence, $1.0 \leqslant P/D \leqslant 2.0$ and $\alpha \geqslant 30^\circ$, the shear-layers from the upstream cylinder do not have sufficient space to roll up completely before being entrained into the wake of the downstream cylinder. In this flow regime the shear-layers from the downstream cylinder form regular Kármán vortices almost without interruption. In the near wake region the Kármán vortices from the inner side of the downstream cylinder are paired with smaller-scale vortices of opposite sign from the inner shear-layer of the upstream cylinder. A little further downstream this vortex pair is enveloped by the outer shear-layer of the upstream cylinder,

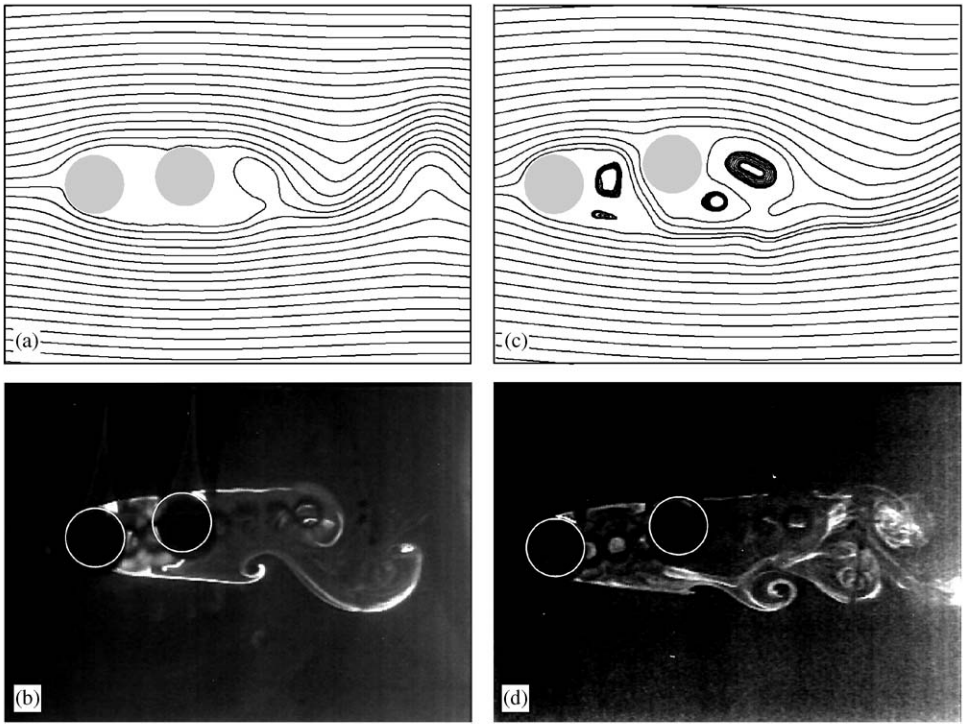

Fig. 6. Comparison of numerical and experimental flow visualization results for staggered cylinders at small angles of incidence: (a) streamline plot from the numerical simulation for $P/D = 1.5$, $\alpha = 5^\circ$, $\mathrm{Re} = 800$; (b) experimental flow visualization for $P/D = 1.5$, $\alpha = 10^\circ$, $\mathrm{Re} = 1300$; (c) streamline plot from the numerical simulation for $P/D = 2.0$, $\alpha = 10^\circ$, $\mathrm{Re} = 800$; (d) experimental flow visualization for $P/D = 2.0$, $\alpha = 10^\circ$, $\mathrm{Re} = 880$. Experimental results taken from Sumner et al. (2000).

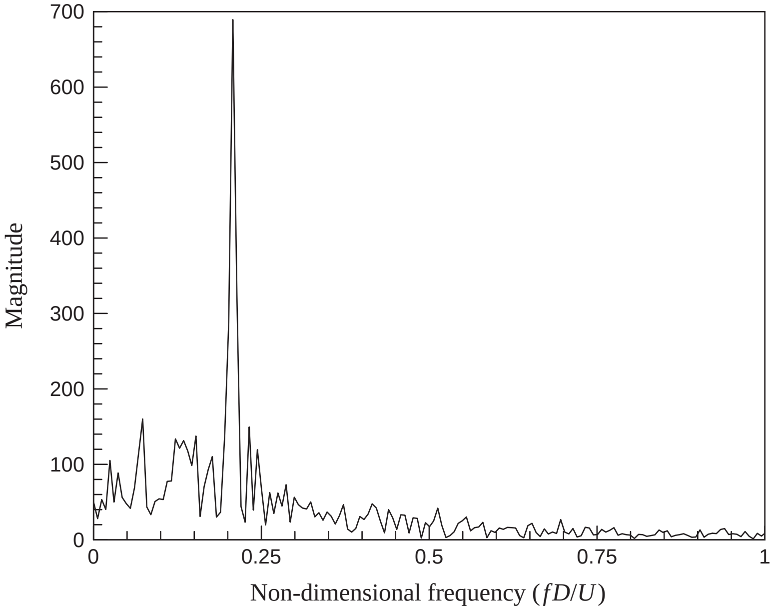

Fig. 7. Wake PSD for $P/D = 1.5$, $\alpha = 5^\circ$, $\mathrm{Re} = 800$, for which the shear-layer reattachment flow pattern was observed in the numerical simulation. Velocity measurement at $x/D = 1.0$ and $y/D = 1.0$ as indicated in Fig. 2.

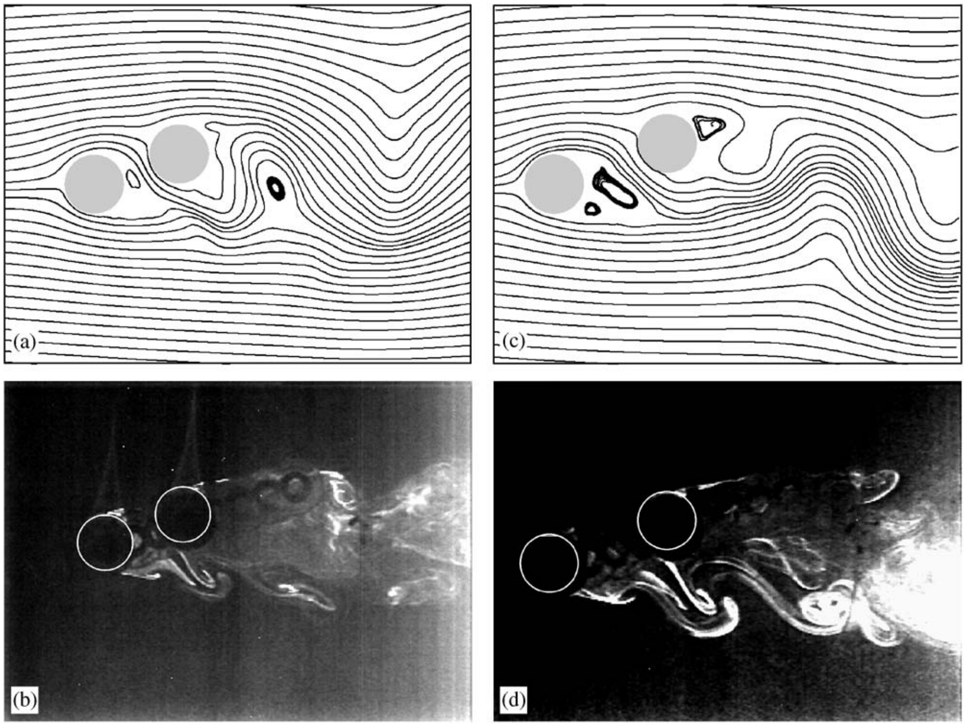

Fig. 8. Comparison of numerical and experimental flow visualization results for staggered cylinders at small angles of incidence: (a) streamline plot from the numerical simulation for $P/D = 2.0$, $\alpha = 20^\circ$, $\mathrm{Re} = 800$; (b) experimental flow visualization for $P/D = 2.0$, $\alpha = 20^\circ$, $\mathrm{Re} = 1320$; (c) streamline plot from the numerical simulation for $P/D = 2.0$, $\alpha = 20^\circ$, $\mathrm{Re} = 800$; (d) experimental flow visualization for $P/D = 2.0$, $\alpha = 20^\circ$, $\mathrm{Re} = 850$. Experimental results taken from Sumner et al. (2000).

before the pair breaks up and the smaller-scale vortex is fully entrained into a like-sign Kármán vortex originating from the outer side of the downstream cylinder. The outer shear-layer of the upstream cylinder partially merges with a like-sign Kármán vortex further downstream in the wake, or eventually fades out. In this flow regime there is one Kármán vortex street in the wake of the two cylinders, although the vortex street is not as regular as that for a single cylinder.

As an example of this flow regime, a sequence of vorticity contour plots is shown in Fig. 9 for $P/D = 2.0$ and $\alpha = 40^\circ$; the corresponding numerical flow visualization plots (streaklines) are presented in Fig. 10. The time-interval between successive frames in these figures is $t^* = 1.0$. Taking the Strouhal number for this case as $\mathrm{St} \approx 0.19$ (discussed later), $t^* = 1.0$ is about one-fifth of the period for one complete vortex shedding cycle in the combined wake of the cylinders. Figs. 9(a, b) and 10(a, b) show the vortex pairing process during one period of vortex shedding for the downstream cylinder. The development of this vortex pair can be followed in Figs. 9(c–f) and 10(c–f). In Figs. 9(e) and 10(e) the break up of the vortex pair, and in Figs. 9(f, g) and 10(f, g) the merging of the smaller-scale vortex with a like-sign Kármán vortex can be observed. A similar process of vortex pairing and break up can be followed in Figs. 9(g–j) and 9(i–l) (and the corresponding Figs. 10(g–j) and 10(i–l)). In Figs. 9(g) and 10(g) the vortex enveloping process is indicated, and a similar process can also be seen in Figs. 9(b), and 9(j, k) (and the corresponding streamline plots in Figs. 10(b), and 10(j, k)). The outer shear-layer from the upstream cylinder merges with a like-sign Kármán vortex from the downstream cylinder in Figs. 9(c, l) and 10(c, l).

The flow structure for this case is compared with corresponding experimental flow visualization results of Sumner et al. (2000) in Figs. 11(a, b). The pairing of vortices and their enveloping by the outer shear-layer of the upstream cylinder is easily identifiable in the corresponding images. Shown in Figs. 11(c, d) are the numerical and experimental flow visualization results for a configuration with $P/D = 1.5$ and $\alpha = 30^\circ$, for which the phenomena of vortex pairing and enveloping is also observed. In this case, as in the previous case, very similar flow patterns are observed in the corresponding images from the numerical simulation and experimental flow visualization.

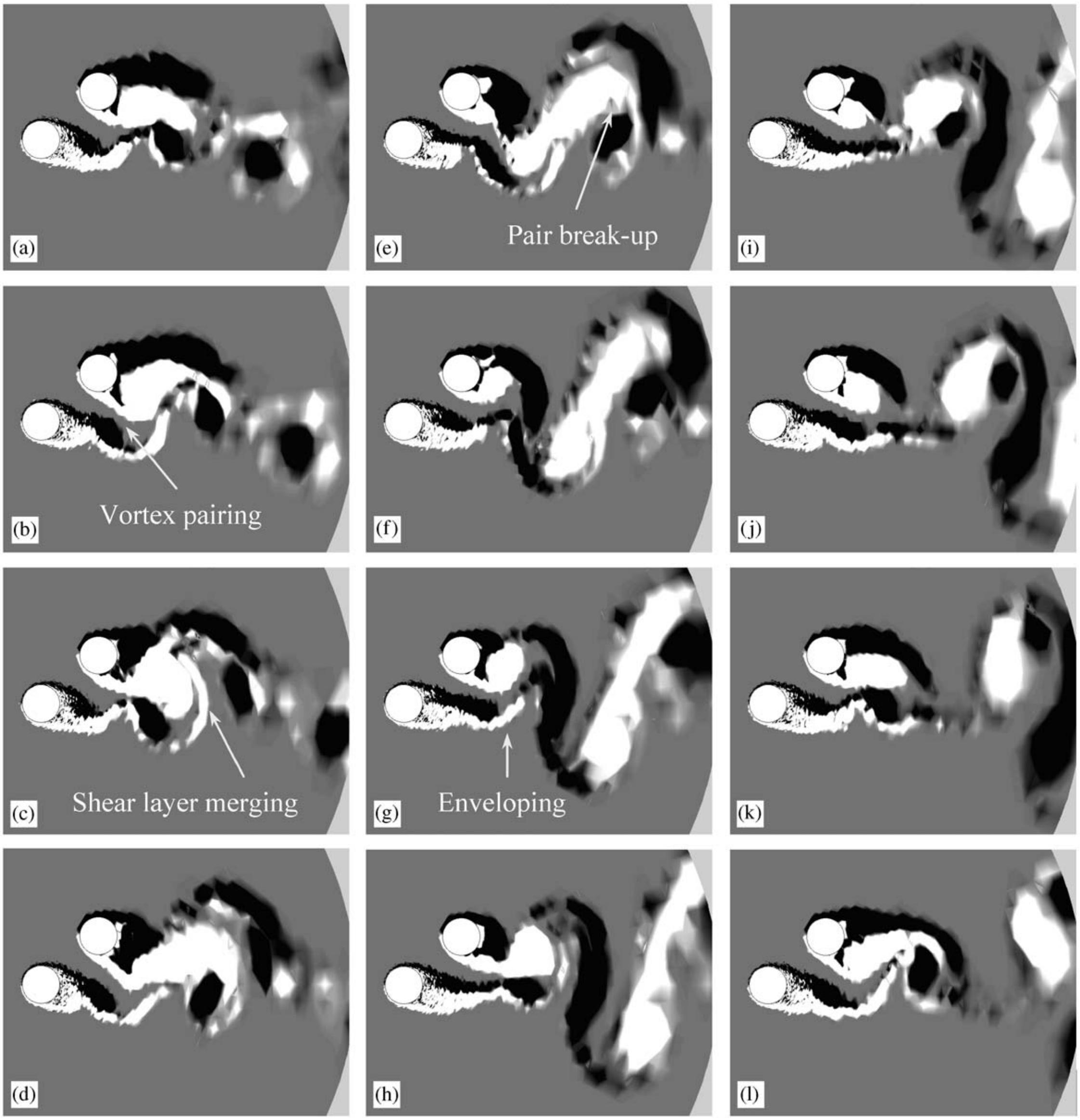

Fig. 9. Vorticity contour plots for a "vortex pairing and enveloping" flow regime with $P/D = 2.0$, $\alpha = 40^{\circ}$, $\mathrm{Re} = 800$. Equal time-intervals of $t^{*} \equiv tU/D = 1.0$ between consecutive plots (a)–(l).

The numerical wake PSD for this case is presented in Fig. 12. The time-trace of the x-velocity component (in the main flow direction) at $x/D = 1.0$ and $y/D = 0.5$, as indicated in Fig. 2, is used to obtain this power spectrum. A dominant nondimensional frequency of about 0.19 is observed, which is attributed to the overall frequency of the vortex shedding in the combined wake of the two cylinders, hence $\mathrm{St} \approx 0.19$. Sumner et al. (2000) reported two Strouhal numbers of $\mathrm{St} \approx 0.14$ and 0.42 for a similar case at a Reynolds number of $\mathrm{Re} = 880$. This considerable discrepancy may be due to the high sensitivity of the wake PSD to the exact location at which the signal is obtained. For example, in this case the higher-frequency shedding from the upstream cylinder, which is apparent in the corresponding flow visualization animation video, is completely absent in the wake PSD shown in Fig. 12. On the other hand, when the velocity at a different location ($x/D = 1.0$ and $y/D = 0.0$) is used to obtain the wake PSD, then a dominant nondimensional frequency of about 0.37 is observed. This frequency appears to be a harmonic of the frequency (of less than 0.19) obtained at another point in the wake, as mentioned previously.

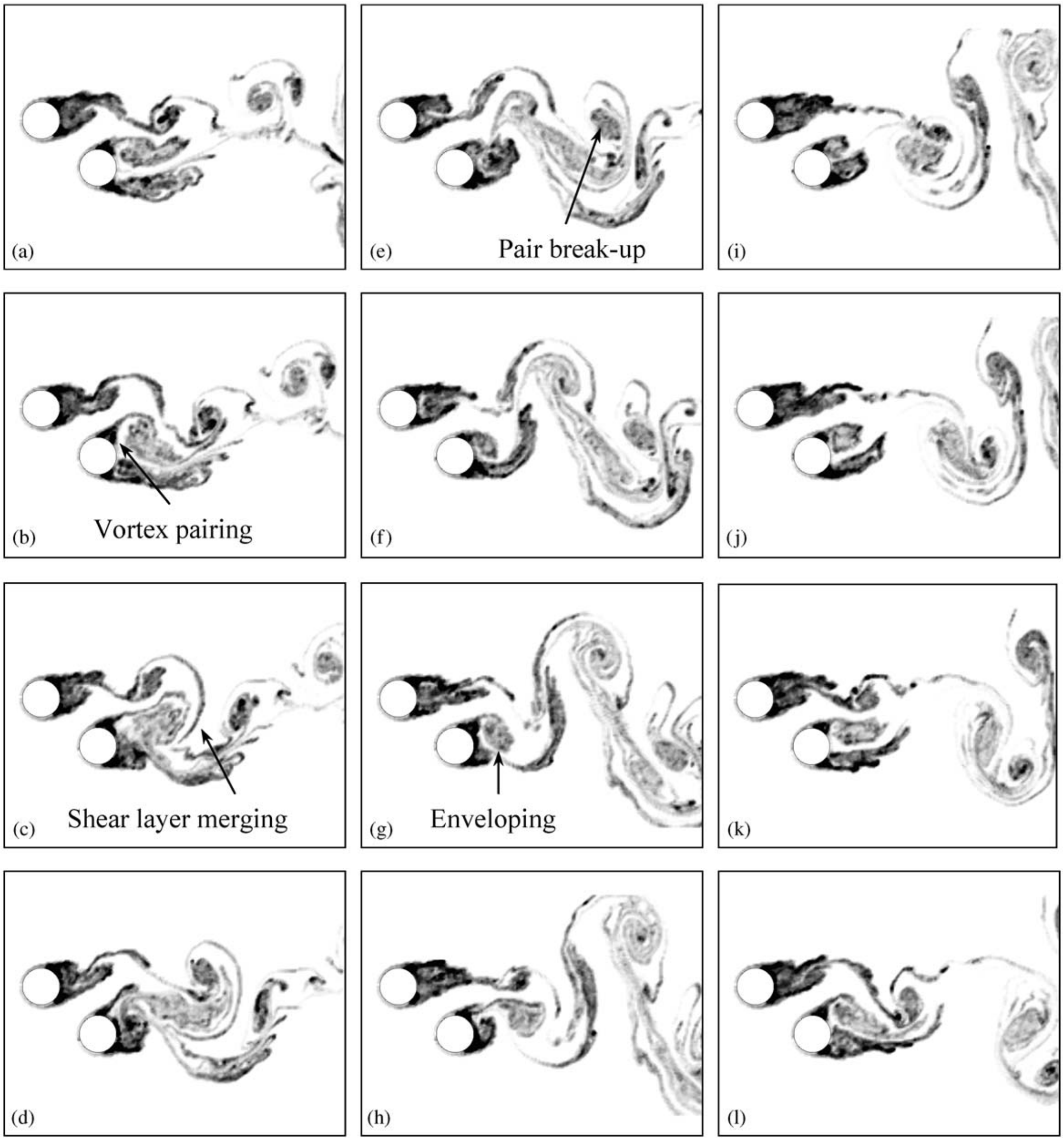

Fig. 10. Flow visualization plots (streaklines) for a "vortex pairing and enveloping" flow regime with $P/D = 2.0$, $\alpha = 40^\circ$, Re = 800. Equal time-intervals of $t^* \equiv tU/D = 1.0$ between consecutive plots (a)–(l).

3.4. Vortex Impingement

This flow regime occurs for configurations with a few cylinder diameters between the two cylinders and where the downstream cylinder is submerged in the wake of the upstream cylinder, i.e., pitch ratios of $P/D \geqslant 3$ and small angles of incidence, $\alpha \leqslant 10^\circ$. There is complete formation of Kármán vortices from the upstream cylinder and these impinge on the downstream cylinder. Because of this impingement, vortex shedding from the downstream cylinder itself is very much disturbed and ceases to be complete. Therefore, the main characteristic of this flow regime is regular vortex shedding from the upstream cylinder, and disturbed, incomplete vortex shedding from the downstream cylinder. The Kármán vortices from the inner side of the upstream cylinder impinge on the downstream cylinder and split into two parts. The outer part combines with a like-sign vortex from the outer side of this cylinder, while the inner part pairs up with an opposite-sign vortex on the inner side of the downstream cylinder. This vortex structure on the inner side of the

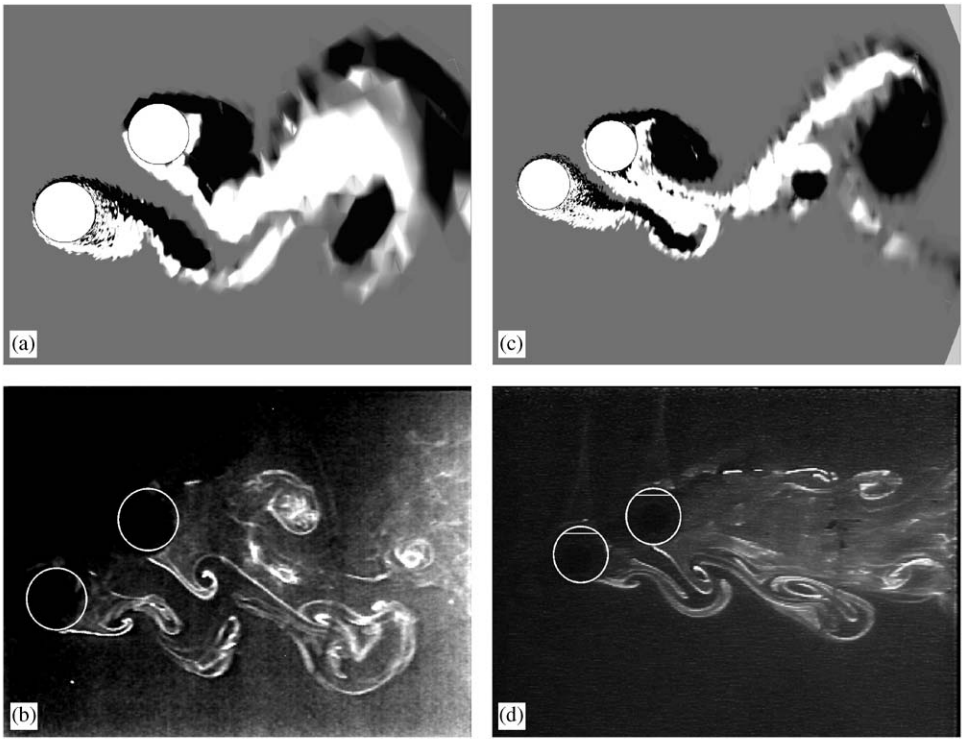

Fig. 11. Comparison of numerical and experimental flow visualization results for staggered cylinders at large angles of incidence: (a) vorticity contour plot from the numerical simulation for $P/D = 2.0$, $\alpha = 40^\circ$, $\mathrm{Re} = 800$; (b) experimental flow visualization for $P/D = 2.0$, $\alpha = 40^\circ$, $\mathrm{Re} = 880$; (c) vorticity contour plot from the numerical simulation for $P/D = 1.5$, $\alpha = 30^\circ$, $\mathrm{Re} = 800$; (d) experimental flow visualization for $P/D = 1.5$, $\alpha = 30^\circ$, $\mathrm{Re} = 850$. Experimental results taken from Sumner et al. (2000).

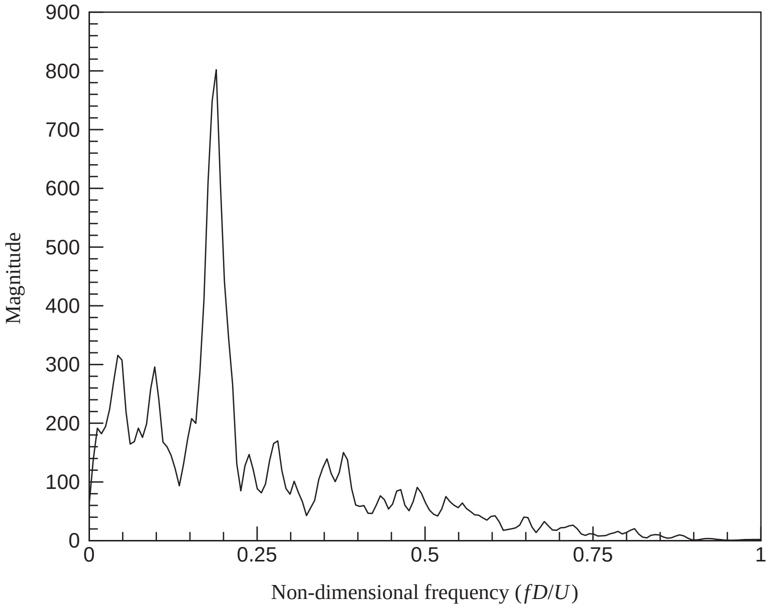

Fig. 12. Wake PSD for $P/D = 2.0$, $\alpha = 40^\circ$, $\mathrm{Re} = 800$, for which the vortex pairing and enveloping flow pattern was observed in the numerical simulation. Velocity measurement at $x/D = 1.0$ and $y/D = 0.5$ as indicated in Fig. 2.

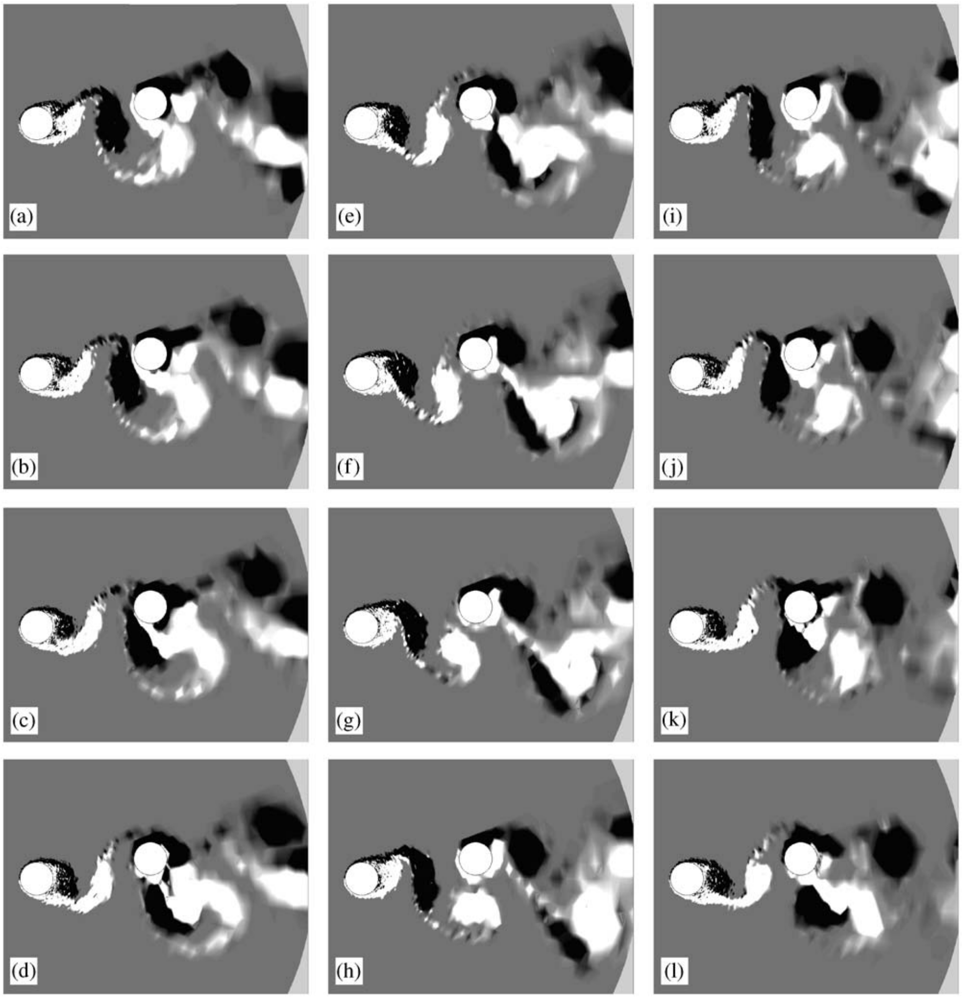

Fig. 13. Vorticity contour plots for a “vortex impingement” flow regime with $P/D = 3.5$, $\alpha = 10^\circ$, Re = 800. Equal time-intervals of $t^* \equiv tU/D = 0.6$ between consecutive plots (a)–(l).

downstream cylinder is a combination of the outer Kármán vortex from the upstream cylinder and an incomplete Kármán vortex from the inner side of the second cylinder, which is entrained into the larger Kármán vortex as it convects downstream. This process results in the incomplete formation of Kármán vortices from the downstream cylinder. The wake structure in this case is not well organized.

Shown in Fig. 13 are the vorticity contour plots at several instances obtained from the numerical simulation for $P/D = 3.5$ and $\alpha = 10^\circ$, for which the vortex impingement phenomenon was observed; the corresponding numerical flow visualization plots (streaklines) are presented in Fig. 14. The time-interval between consecutive plots in these figures is $t^* = 0.6$, this is about one-eighth of the period for one complete cycle of vortex shedding in the cylinders' wake. The Kármán vortex from the inner side of the upstream cylinder is fully formed in Figs. 13(a) and 14(a), and its impingement on the downstream cylinder is observed in Figs. 13(b–d) and 14(b–d). This vortex splits into two parts upon impingement (Figs. 13(c) and 14(c)), the outer part of which merges into the shear-layer from the outer surface of the downstream cylinder (Figs. 13(d–f) and 14(d–f)), and the inner part merges into the previously shed opposite-sign Kármán vortex from the outer side of the upstream cylinder (Figs. 13(f–i) and 14(f–i)). This process prevents the regular formation of Kármán vortices from the downstream cylinder, as seen in Figs. 13(c–f) and 13(j–l) (and the corresponding Figs. 14(c–f) and 14(j–l)).

Three dominant frequencies are observed in the wake PSD for this case, shown in Fig. 15 for $x/D = 1.0$ and $y/D = 1.0$; these (dimensionless) frequencies are at $fD/U \approx 0.1, 0.2$, and 0.4. The peaks at 0.4 and 0.1 are almost certainly the 1/2-subharmonic and 2-superharmonic, respectively, of the peak at 0.2. Sumner et al. (2000) did not report

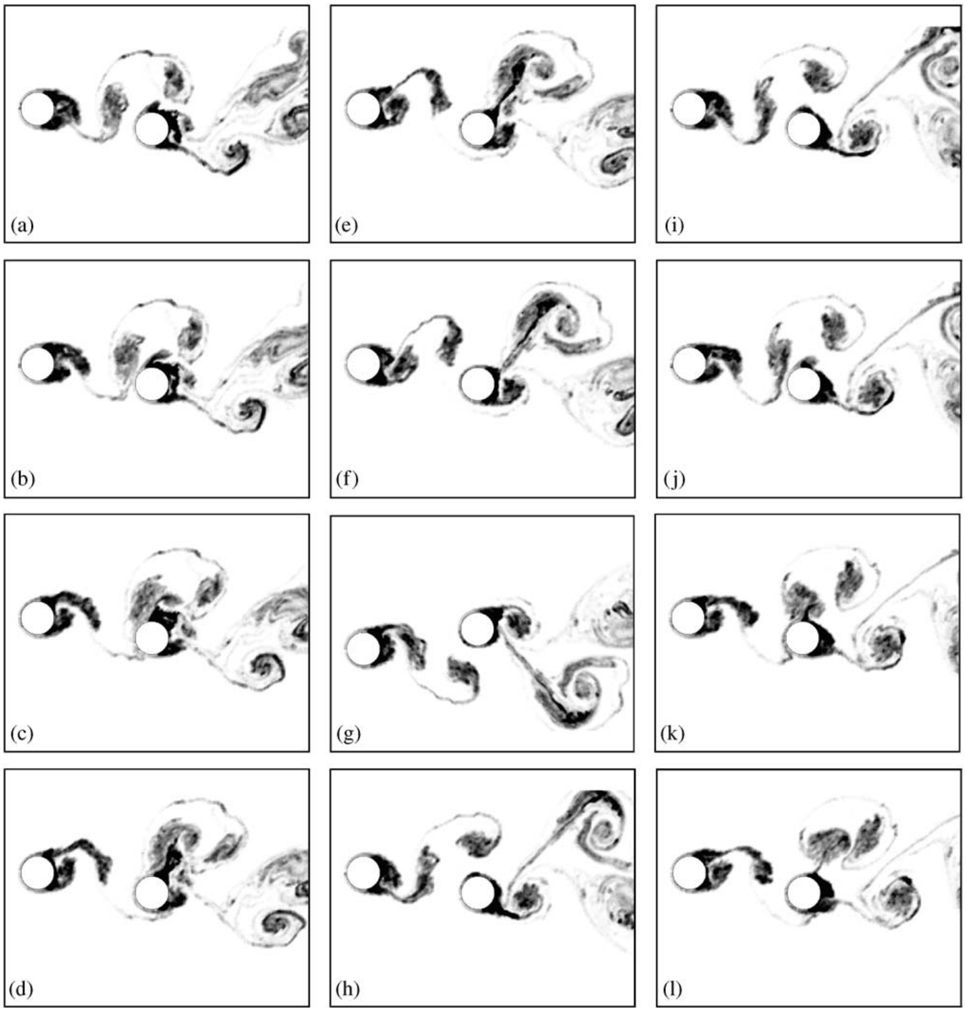

Fig. 14. Flow visualization plots (streaklines) for a "vortex impingement" flow regime with $P/D = 3.5$, $\alpha = 10^\circ$, $\mathrm{Re} = 800$. Equal time-intervals of $t^* \equiv tU/D = 0.6$ between consecutive plots (a)–(l).

a Strouhal number for a similar case in their experiments, however Moriya and Sakamoto (1985) reported a Strouhal number of $\mathrm{St} \approx 0.18$ for a similar configuration at a Reynolds number of 65 300. It is appreciated, of course, that there will be significant differences between the experimental flow of Moriya and Sakamoto (1985) at $\mathrm{Re} = 65\,300$ and the present simulation at $\mathrm{Re} = 800$; however, given the lack of experimental data at a more appropriate Reynolds number, this does provide a qualitative comparison.

3.5. Complete Vortex Shedding

This phenomenon occurs for configurations where the downstream cylinder is not immersed in the wake of the upstream cylinder, but where the two cylinders are close enough for them to influence the vortex shedding from each other. Cylinder configurations with $P/D \geqslant 2.5$ and high angles of incidence ($\alpha \geqslant 30^\circ$) can experience this phenomenon. In this flow regime each cylinder sheds Kármán vortices of its own, hence two distinct Kármán vortex streets are seen in the wake of the cylinder pair. However, the vortex shedding frequency of at least the upstream cylinder is higher than that for a single cylinder in a cross-flow. This may be attributed to the narrower near wake of the cylinder, hence shorter time for the shear-layers to roll up and form Kármán vortices. For some configurations the like-sign Kármán vortices from the two cylinders coalesce further downstream in the wake and form large-scale vortex structures.

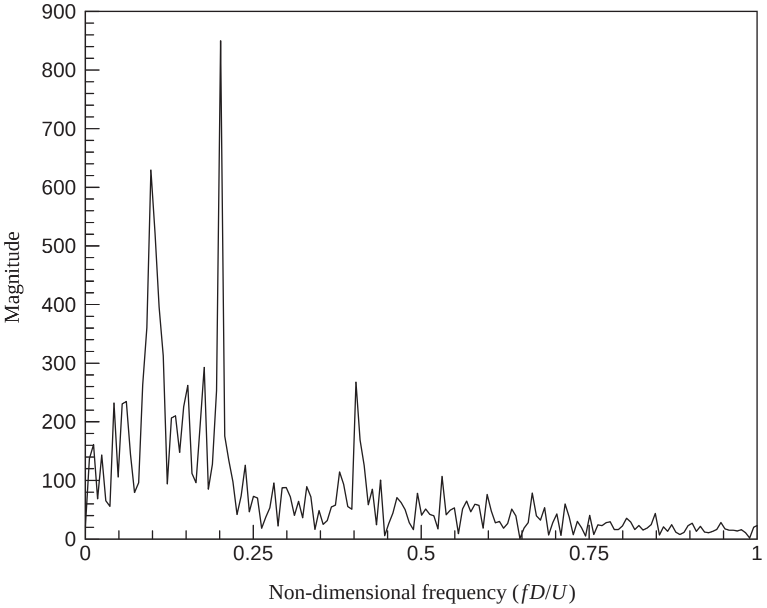

Fig. 15. Wake PSD for $P/D = 3.5$, $\alpha = 10°$, $\mathrm{Re} = 800$, for which the vortex impingement flow pattern was observed in the numerical simulation. Velocity measurement at $x/D = 1.0$ and $y/D = 1.0$ as indicated in Fig. 2.

In all simulations for different cylinder configurations exhibiting this flow pattern, the frequency of vortex shedding from the two shear-layers of the same cylinder is always the same. This is in contrast to what is reported by Sumner et al. (2000), who suggest that for this configuration, referred to as "synchronized vortex shedding", a higher shedding frequency exists for three of the shear-layers (the inner shear-layer of the downstream cylinder and those of the upstream cylinder) compared with the other. Sumner et al. noted that this flow pattern was marked by the synchronization of the gap-vortices from the inner sides of the two cylinders. The numerical simulations exhibited a similar phenomenon for only *some* of the cylinder configurations where Sumner et al. (2000) reported this synchronization; more details are given later in this section.

Shown in Fig. 16 are the vorticity contour plots for $P/D = 2.5$ and $\alpha = 50°$, with time-intervals of $t^* = 1.0$ between successive plots. The corresponding numerical flow visualization plots (streaklines) are presented in Fig. 17. It is observed in Figs. 16(a) and 17(a) that at this particular instant there are two pairs of Kármán vortices in the wake of the two cylinders. Also, the release of the most recent Kármán vortex (A) from the upstream cylinder is seen in these figures. It is clearly seen in Figs. 16(b–e) and 17(b–e) that this Kármán vortex (A) is not paired with another vortex from the other cylinder. This shows that the gap-vortices shed from the two cylinders are not synchronized for this configuration. On the other hand, in Figs. 16(e, h, l) and 17(e, h, l) it may seem that gap-vortices from the two cylinders are paired. However, a careful review of the animation video for this case reveals that the two cylinders do not shed vortices at the same frequency, but the frequencies are close enough that this misinterpretation may easily occur.

In fact, by counting the number of vortices shed in a relatively long period of time ($t^* = 250$), the Strouhal number for the upstream cylinder turns out to be $\mathrm{St} \approx 0.22$, and that for the downstream cylinder to be $\mathrm{St} \approx 0.175$. These relatively close Strouhal numbers for the two cylinders may explain the apparent synchronization of vortex shedding from the cylinders. It is also observed that the Strouhal number for the upstream cylinder is higher than that for a single cylinder in a cross-flow at the same Reynolds number ($\mathrm{St} \approx 0.185$ in our simulation). The wake PSD for this case is presented in Fig. 18, where two dominant frequencies are observed at $fD/U \approx 0.22$ and 0.29; a peak at $fD/U \approx 0.52$ is also observed in the PSD. The peak at 0.22 corresponds to the Strouhal number for the upstream cylinder. The peak at 0.52 is possibly the 1/3-subharmonic of the vortex shedding frequency of the downstream cylinder; or, it may be due to the smaller-scale vortices resulting from Kelvin–Helmholtz instability in the shear-layers from the cylinders (Unal and Rockwell, 1988). These vortices are visible in the near wake region of the flow visualization results of Fig. 17. The cause of the peak at 0.29 is not obvious to us.

For a configuration with $P/D = 2.5$ and $\alpha = 70°$, the Strouhal numbers for the upstream and downstream cylinders were found to be $\mathrm{St} \approx 0.22$ and 0.2, respectively. In this case, the vortex shedding frequency from the upstream cylinder

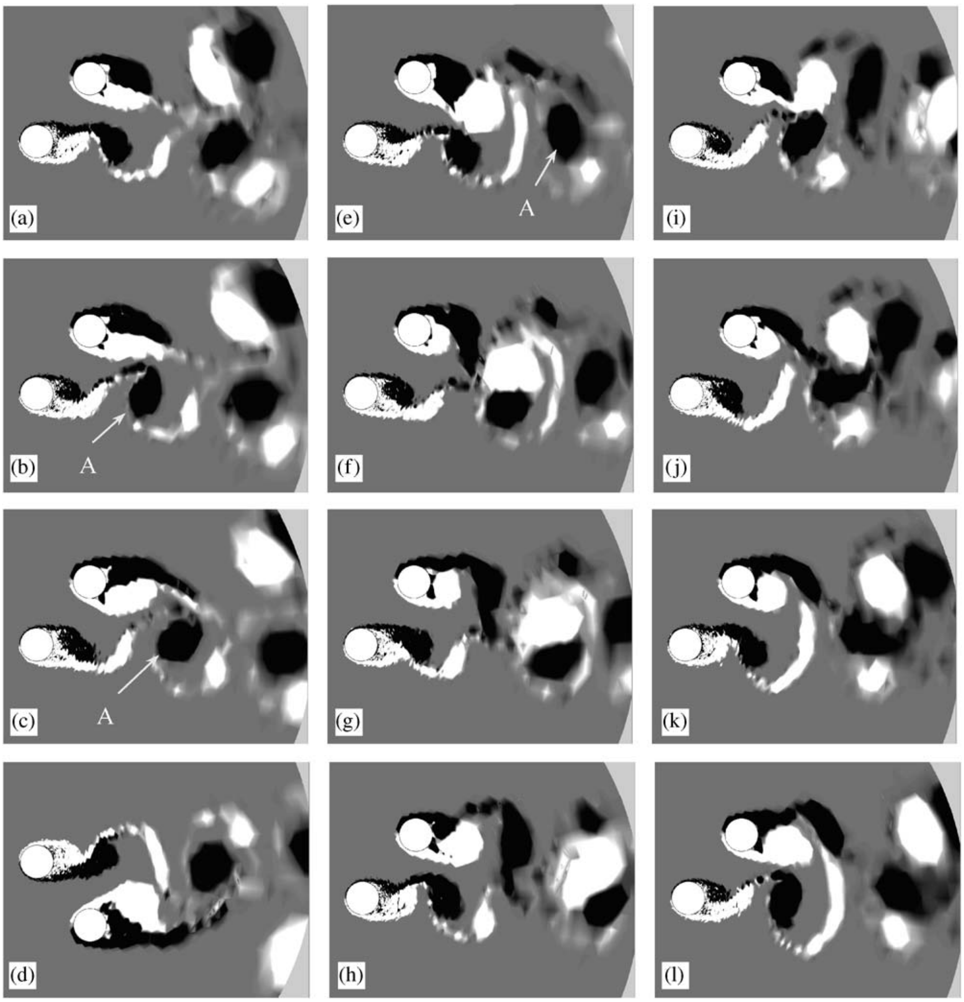

Fig. 16. Vorticity contour plots for a "complete vortex shedding" flow regime with $P/D = 2.5$, $\alpha = 50^\circ$, $\mathrm{Re} = 800$. Equal time-intervals of $t^* \equiv tU/D = 1.0$ between consecutive plots (a)–(l).

is the same as for the previous case with a smaller angle of incidence ($\alpha = 50^\circ$). On the other hand, the shedding frequency for the downstream cylinder is higher compared to the previous case, and is closer to that for the upstream cylinder.

For a case with $P/D = 3.5$ and $\alpha = 30^\circ$, the two cylinders have equal Strouhal numbers of $\mathrm{St} \approx 0.175$ in our simulation. The Strouhal number for the upstream cylinder in this case is lower compared to the two previous cases with smaller distances between the two cylinders. Vorticity contour plots at several instances are shown in Fig. 19, and the corresponding numerical flow visualization plots (streaklines) are shown in Fig. 20. The pairing of gap-vortices can be seen in Figs. 19(a, e, j) and 20(a, e, j). For this configuration there are four distinct rows of Kármán vortices in the wake of the cylinders, with two opposite-sign vortices paired in the middle. However, it is not clear whether this pairing of gap-vortices is simply because of the "right" longitudinal distance between the two cylinders, or that there is a synchronization mechanism involved in this process.

Numerical flow visualization results for two configurations are compared with their corresponding experimental results in Fig. 21. As shown in Figs. 21(a, c) the two gap-vortices seem to be pairing in our numerical results for both configurations, which is also the case in the corresponding experimental results shown in Figs. 21(b, d). However, as mentioned previously, a more careful review of the numerical results for the case shown in Fig. 21(a) discloses that this vortex pairing occurs only during some instances, and that there is no synchronization of vortex shedding between the two cylinders. Also, as previously mentioned, the vortex shedding synchronization for the two cylinders

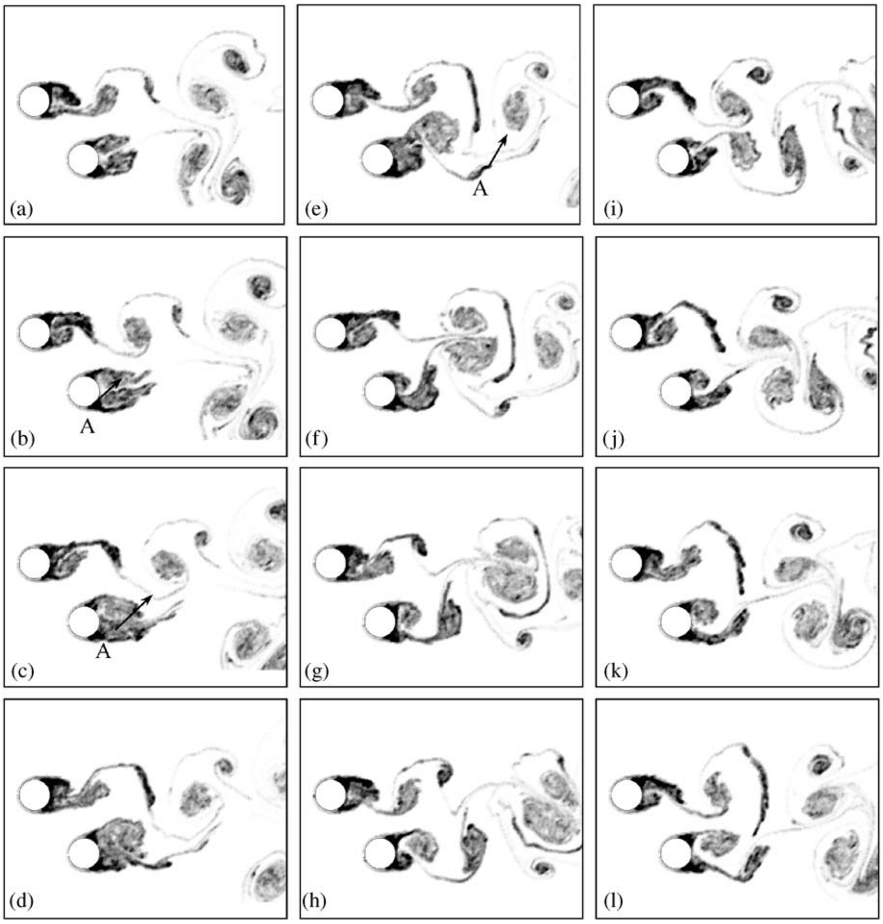

Fig. 17. Flow visualization plots (streaklines) for a “complete vortex shedding” flow regime with $P/D = 2.5$, $\alpha = 50^\circ$, Re = 800. Equal time-intervals of $t^* \equiv tU/D = 1.0$ between consecutive plots (a)–(l).

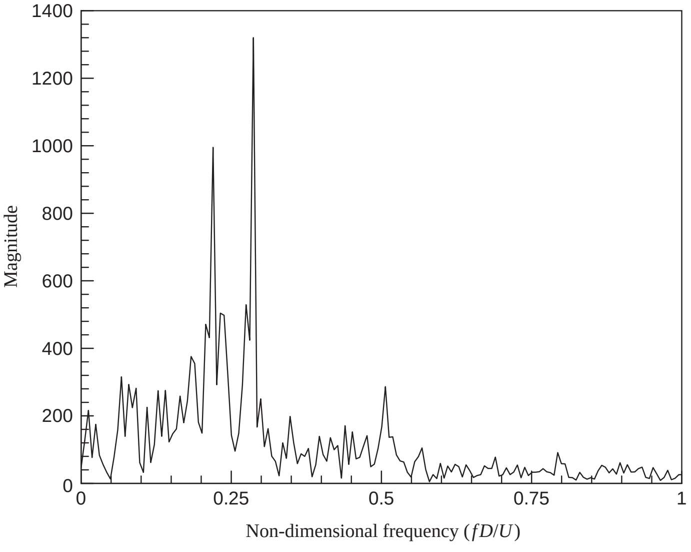

Fig. 18. Wake PSD for $P/D = 2.5$, $\alpha = 50^\circ$, Re = 800, for which the complete vortex shedding flow pattern was observed in the numerical simulation. Velocity measurement at $x/D = 2.0$ and $y/D = 0.5$ as indicated in Fig. 2.

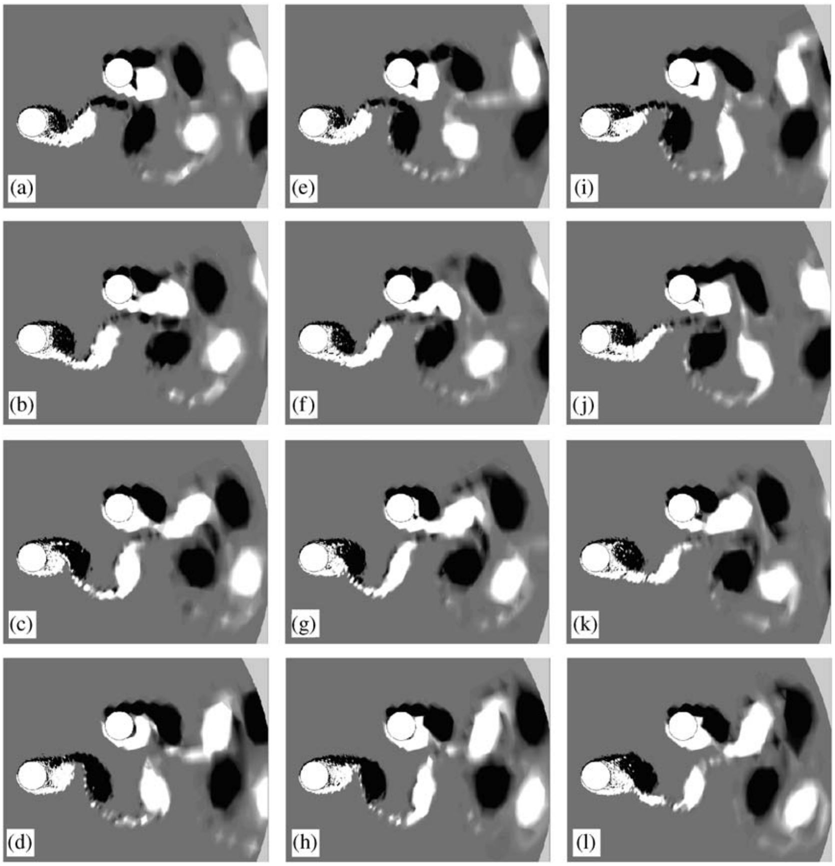

Fig. 19. Vorticity contour plots for a "complete vortex shedding" flow regime with $P/D = 3.5$, $\alpha = 30^\circ$, $\mathrm{Re} = 800$. Equal time-intervals of $t^* \equiv tU/D = 1.0$ between consecutive plots (a)–(l).

in Fig. 21(c) may simply be a consequence of the specific spacing between the cylinders. This is supported by the fact that no such synchronization is observed in our simulations in the other cases presented in this section, or even with smaller pitch ratios.

4. Conclusions

Five distinct flow patterns are identified for a pair of circular cylinders in different staggered configurations in the low subcritical Reynolds number regime, $\mathrm{Re} = 800$. The numerical observations made in this study are supported by previous experimental results. For configurations with very small pitch ratios of $P/D \leqslant 1.1$ and relatively high angles of incidence, $\alpha \geqslant 30^\circ$, the "base-bleed" (BB) flow is observed, where a high-speed gap-flow prevents formation of regular vortex shedding from the upstream cylinder, hence a disorganized near-wake for the cylinder pair.

The "shear-layer reattachment" (SLR) flow regime is observed for configurations with relatively small pitch ratios and small angles of incidence, $P/D < 2.0$ and $\alpha < 10^\circ$. The inner shear-layer from the upstream cylinder reattaches on the outer side of the downstream cylinder, which then minimizes the gap-flow between the cylinders. There is one Kármán vortex street in the wake of the cylinders, similar to that for a single bluff-body.

For configurations with similar pitch ratios ($P/D \leqslant 2.0$) but high angles of incidence, $\alpha \geqslant 30^\circ$, the "vortex pairing and enveloping" (VPE) phenomenon is observed. In this flow regime the downstream cylinder sheds Kármán vortices almost regularly, while the shear-layers from the upstream cylinder do not have sufficient space to roll up completely

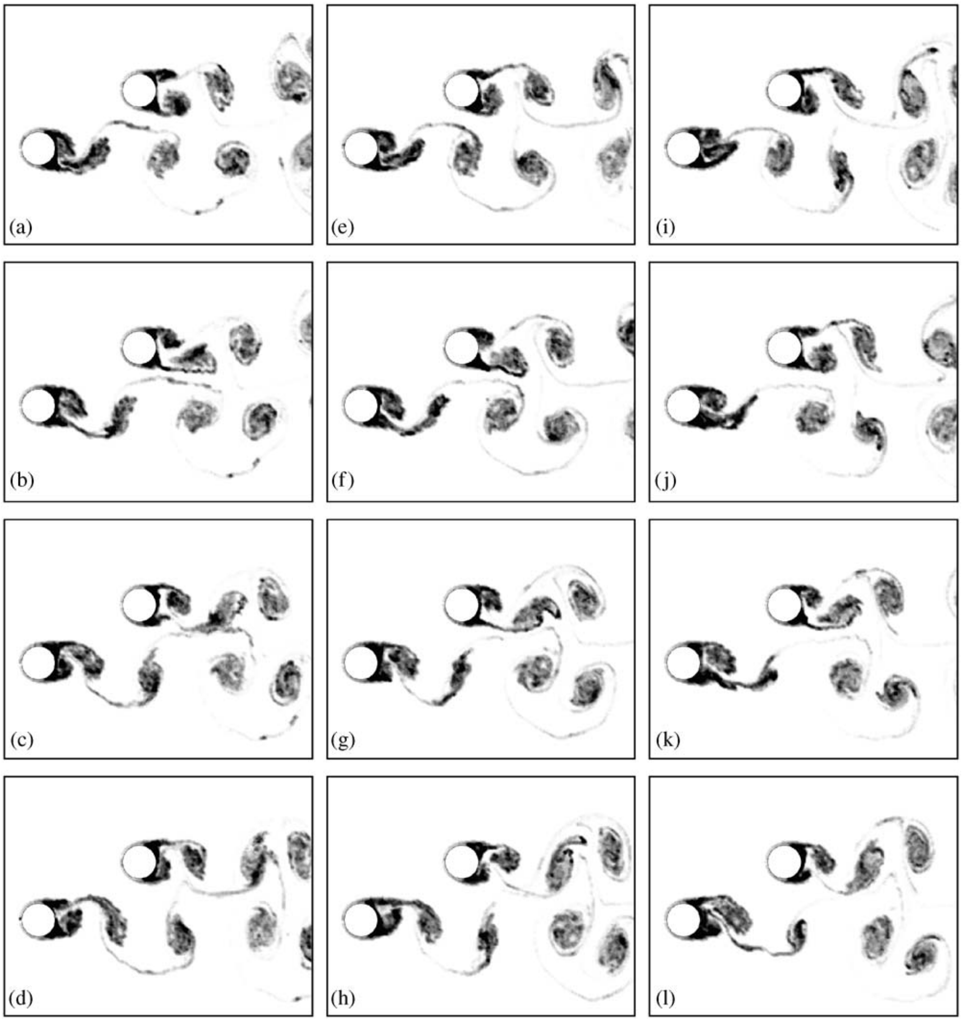

Fig. 20. Numerical flow visualization plots (streaklines) for a "complete vortex shedding" flow regime with $P/D = 3.5$, $\alpha = 30^\circ$, $\mathrm{Re} = 800$. Equal time-intervals of $t^* \equiv tU/D = 1.0$ between consecutive plots (a)–(l).

and form large-scale Kármán vortices of their own. Instead, the inner shear-layer forms smaller-scale vortices that then pair up with the inner Kármán vortex of the downstream cylinder, and the outer shear-layer envelopes this vortex pair and further downstream is entrained into the like-sign Kármán vortex from the downstream cylinder. The wake from the pair of cylinders is wider and less organized for this flow regime compared with the others.

The "vortex impingement" (VI) flow regime occurs for cylinder configurations with large pitch ratios, $P/D \geqslant 3.0$, and small angles of incidence, $\alpha \leqslant 10^\circ$. The downstream cylinder is immersed in the wake of the upstream cylinder in this flow regime. The inner Kármán vortices from the upstream cylinder impinge on the downstream cylinder and split into two parts. The outer Kármán vortices from the upstream cylinder convect near the inner side of the second cylinder and entrain the incomplete Kármán vortices from this cylinder. Vortex shedding from the downstream cylinder is disrupted and incomplete, and the wake structure is not well organized.

Finally, for cylinder configurations with relatively large pitch ratios, $P/D \geqslant 2.5$, and large angles of incidence, $\alpha \geqslant 30^\circ$, the "complete vortex shedding" (CVS) flow regime is observed in the simulations. In this case both cylinders shed Kármán vortices regularly, and the wake structure contains three or four rows of vortex structures. Compared with an isolated single cylinder the upstream cylinder exhibits higher-frequency vortex shedding, while the vortex shedding frequency for the downstream cylinder may be lower or higher. In some cases, like-sign vortices may coalesce further downstream in the wake, forming large-scale vortex structures.

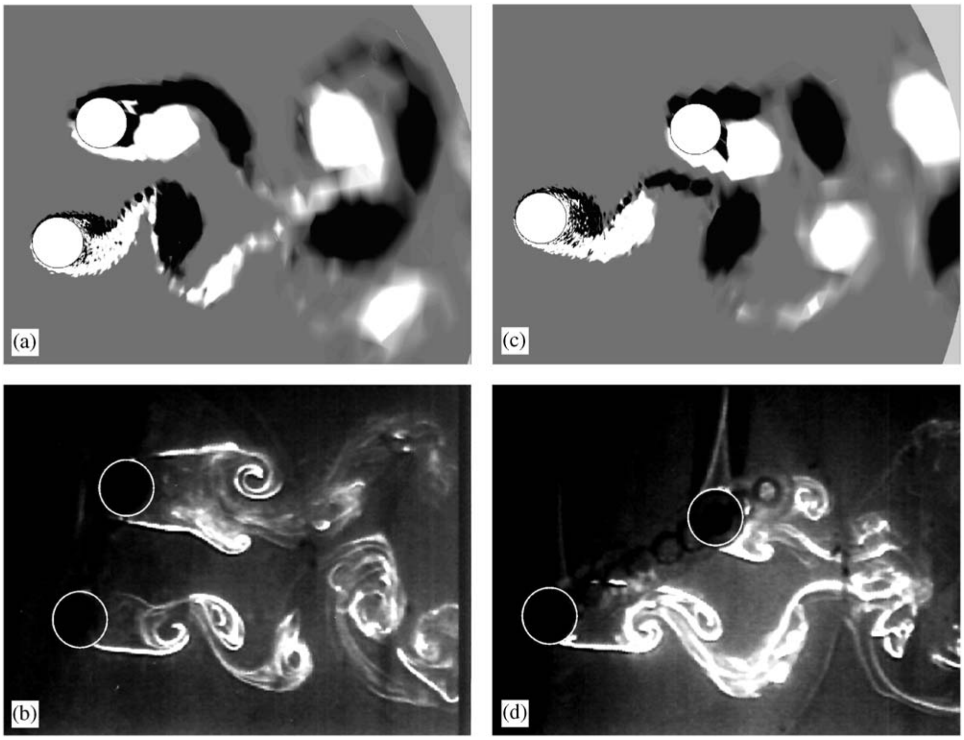

Fig. 21. Comparison of numerical and experimental flow visualization results for staggered cylinders at large pitch ratios: (a) vorticity contour plot from the numerical simulation for $P/D = 2.5$, $\alpha = 70^\circ$, $\mathrm{Re} = 800$; (b) experimental flow visualization for $P/D = 2.5$, $\alpha = 70^\circ$, $\mathrm{Re} = 900$; (c) vorticity contour plot from the numerical simulation for $P/D = 3.5$, $\alpha = 30^\circ$, $\mathrm{Re} = 800$; (d) experimental flow visualization for $P/D = 3.5$, $\alpha = 30^\circ$, $\mathrm{Re} = 830$. Experimental results taken from Sumner et al. (2000).

Acknowledgements

The authors would like to gratefully acknowledge the financial support of the National Science and Engineering Research Council of Canada (NSERC). The authors also wish to thank Dr D. Sumner for providing the experimental flow visualization images used in this paper.

References

Akbari, M.H., 1999. Bluff-body flow simulations using vortex methods. Ph.D. Thesis, Department of Mechanical Engineering, McGill University, Montréal, Canada.

Akbari, M.H., Price, S.J., 1997. Simulation of the incompressible viscous cross-flow around an oscillating circular cylinder via the random vortex method. In: Païdoussis, M.P., et al. (Eds.), Proceedings of the Fourth International Symposium on Fluid–Structure Interactions, Aeroelasticity, Flow-Induced Vibration and Noise, AD-vol. 531. ASME, New York, pp. 21–32.

Akbari, M.H., Price, S.J., 2000. Simulation of the flow over elliptic airfoils oscillating at large angles of attack. Journal of Fluids and Structures 14, 757–777.

Akbari, M.H., Price, S.J., 2003. Simulation of dynamic stall for a NACA 0012 airfoil using a vortex method. Journal of Fluids and Structures 17, 855–874.

Bearman, P.W., 1967. The effect of base bleed on the flow behind a two-dimensional model with a blunt trailing edge. The Aeronautical Quarterly 18, 207–224.

Chorin, A.J., 1973. Numerical study of slightly viscous flows. Journal of Fluid Mechanics 57, 785–796.

Gu, Z.F., Sun, T.F., 1999. On interface between two circular cylinders in staggered arrangement at high subcritical Reynolds numbers. Journal of Wind Engineering and Industrial Aerodynamics 80, 287–309.

Ishigai, S., Nishikawa, E., Nishimura, K., Cho, K., 1972. Experimental study of structure of gas flow in tube banks with tube axes normal to flow (Part I, Kármán vortex flow from two tubes at various spacings). Bulletin of JSME 15, 949–956.

Jester, W., Kallinderis, Y., 2003. Numerical study of incompressible flow about fixed cylinder pairs. Journal of Fluids and Structures 17, 561–577.

Kiya, M., Arie, M., Tamura, H., Mori, H., 1980. Vortex shedding from two circular cylinders in staggered arrangement. Transactions of ASME: Journal of Fluids Engineering 102, 166–173.

Mittal, S., Kumar, V., Raghuvanshi, A., 1997. Unsteady incompressible flows past two cylinders in tandem and staggered arrangements. International Journal of Numerical Methods in Fluids 25, 1315–1344.

Moriya, M., Sakamoto, H., 1985. Fluctuating fluid forces acting on a downstream circular cylinder in the staggered arrangement. Transactions of JSME 51, 2098–2104 (in Japanese).

Price, S.J., 1976. The origin and nature of the lift force on the leeward of two bluff bodies. The Aeronautical Quarterly 27, 154–168.

Price, S.J., Païdoussis, M.P., 1984. The aerodynamic forces acting on groups of two and three circular cylinders when subject to a cross-flow. Journal of Wind Engineering and Industrial Aerodynamics 17, 329–347.

Smith, P.A., Stansby, P.K., 1989. Postcritical flow around a circular cylinder by the vortex method. Journal of Fluids and Structures 3, 275–291.

Su, Z., Liu, Y., So, R.M.C., 2002. Two staggered elastic cylinders in a cross flow. In: Proceedings of IMECE2002 ASME International Mechanical Engineering Congress and Exposition, New Orleans, LA, USA, IMECE2002-32183, pp. 1–10.

Sumner, D., Price, S.J., Païdoussis, M.P., 2000. Flow-pattern identification for two staggered circular cylinders in cross-flow. Journal of Fluid Mechanics 411, 263–303.

Suzuki, N., Sato, H., Iuchi, M., Yamamoto, S., 1971. Aerodynamic forces acting on circular cylinders arranged in a longitudinal row. In: Wind Effects on Buildings and Structures, International Wind Conference, Tokyo, Part II, pp. 20-1–20-10.

Swarztrauber, P., Sweet, R., 1975. Efficient FORTRAN subprograms for the solution of elliptic partial differential equations. National Center for Atmospheric Research, Boulder, CO, USA, NCAR-TN/IA-109.

Unal, M.F., Rockwell, D., 1988. On vortex formation from a cylinder. Part 1: The initial instability. Journal of Fluid Mechanics 190, 491–512.

Zdravkovich, M.M., 1987. The effects of interference between circular cylinders in cross flow. Journal of Fluids and Structures 1, 239–261.